A Sustainable Natural Clam Shell Derived Photocatalyst for the Effective Adsorption and Photodegradation of Organic Dyes

Hailong Zhang (h_l_zhang@yahoo.com)
Zhejiang Ocean University
Xinxin Yao
Zhejiang Ocean University
Ting Qu
Zhejiang Ocean University
Gary Owens
University of South Australia
Liangjun Gao
Zhejiang Ocean University

Research Article

Keywords: Clam shell, Calcination, Congo red, Methylene blue, Photocatalysis

Posted Date: November 10th, 2021

DOI: https://doi.org/10.21203/rs.3.rs-1039754/v1

A sustainable natural clam shell derived photocatalyst for the effective adsorption and photodegradation of organic dyes

Xinxin Yao [a], Ting Qu [b], Gary Owens [c], Liangjun Gao [a], Hailong Zhang [a]*

[a] Zhejiang Key Laboratory of Petrochemical Environmental Pollution Control, National-Local Joint Engineering Laboratory of Harbor Oil and Gas Storage and Transportation Technology, School of Petrochemical Engineering and Environment, Zhejiang Ocean University, Zhoushan, Zhejiang, 316022, China

[b] National Engineering Research Center for Marine Aquaculture, Institute of Innovation & Application, Zhejiang Ocean University, Zhoushan, Zhejiang, 316022, China

[c] Environmental Contaminants Group, Future Industries Institute, University of South Australia, Mawson Lakes Campus, Mawson Lakes, South Australia, 5095, Australia

* Correspondence: h_l_zhang@yahoo.com (H. Zhang); Tel.: +86-580-226-2589 (H.Z.)

Abstract

In response to the increasing desire for modern industries to be both green and sustainable, there has been increasing research focus on the reutilization of natural waste materials to effectively remove and degrade toxic wastewater effluents. One interesting food industry waste product is clam shells. Here a new photocatalytic nanomaterial derived from marine clam shells was successfully prepared and characterized. Thereafter the material was applied for the removal of two target dyes from aqueous solution, where the effect of both catalyst dose and initial dye concentration on adsorption and photocatalysis properties was investigated. The maximum adsorption capacities of methylene blue (100 mg/L) and Congo red (500 mg/L) were 123.45 mg/g and 679.91 mg/g, respectively, where adsorption followed pseudo second order kinetics predominantly via a chemical adsorption process. The photodegradation removal efficiencies of the two dye solutions under visible light irradiation were 99.6% and 83.3% for MB and CR respectively. These results demonstrated that a clam shell catalyst also exhibited excellent degradation performance in a mixed dye solution with strong degradation capability and low cost, making the material a good candidate for practical field remediation of dye contaminated wastewater.

Keywords:

Clam shell; Calcination; Congo red; Methylene blue; Photocatalysis

1. Introduction

While water is essential for all life, the rapid growth in modern human civilizations globally, concurrent with vigorous and rapid industrialization has resulted in significant pollution of water resources through the discharge of waste materials, especially by the dye industry. Water resource contamination by dye wastewaters is becoming increasingly serious (Chequer et al., 2009). Methylene blue (MB), Congo red (CR) and many other organic dyes are widely and routinely used in large quantities by various dye industries. These dye molecules have a complex molecular structure containing many diverse functional groups such as amino, hydroxyl and the benzene ring (Balakrishnan et al., 2016), which while giving the dye strong coloring ability also result in strong toxicity and poor biodegradability (Chen et al., 2018). These latter features are of concern because the efflux of large concentrations of dyes into the natural environment may thus lead to environmental harm. Hence, development of new materials to treat dye wastewater is urgently required to mitigate environmental pollution. While many non-destructive methods, such as adsorption, membrane filtration, and precipitation, have previously been successfully employed to remove dye from wastewater, the disadvantage of non-destructive methods are that do they nor destroy the dye but merely concentrate the dye into either sludge or silt, which still needs further treatment to remove the hazard (Tsai et al., 2020). In comparison, destructive methods, can directly decompose large dyes into non-toxic smaller molecules, can be directly discharged into the environment. Therefore, of the destructive methods, photocatalytic reduction has emerged as a popular destructive method. For example, bismuth oxychloride nanomaterials were synthesised via a hydrothermal method, and used for the degradation rate of Congo red with a 72% photocatalytic removal efficiency (Ismail et al., 2019). A Fe_2O_3-CeO_2 nanocomposite prepared by a precipitation and improved sol gel self-ignition method, exhibited a 96% photodegradation removal efficiency for CR (Aboutaleb et al., 2019). Ma et al (2017) also successfully synthesized a MgZnCr-TiO_2 nanocomposite photocatalyst by co-precipitation, which removed 99.8% of CR

after 180 min. However, the disadvantage of these artificially synthesized catalysts was that the preparation process was complex and, also required expensive and toxic chemical reagents. The application of nanomaterials for photocatalysis is highly desirable due the nanomaterial's high surface areas and semiconductor heterogeneous structures, which significantly improves dye degradation efficiency. Although many nanoparticles have been reported for effective degradation, there are only a few studies which have considered the preparation of photocatalysts from waste materials. Shariffuddin et al (2018) investigated the feasibility of using CaO derived from cockle shells as catalyst for MB removal and demonstrated good degradation. Likewise, E-CaO nanoparticles derived from waste eggshell were successfully prepared by calcination method for efficient photodegradation of methylene blue (MB) and toluidine blue (TB) (Sree et al., 2020), where preparation of E-CaO was both eco-friendly and sustainable. These two studies clearly indicated that recycling wastes as nanomaterial remediating agents was certainly feasible. Hence, it is expected, that in the ongoing search for more efficient and sustainable degradation of dyes, natural photocatalysts derived from waste biomass waste will provide an economical, sustainable and environmentally friendly method.

Clams are widely distributed in both the North and South Seas of China, where they grow rapidly, with a short breeding cycle and exhibit strong adaptability, thus making them an excellent shellfish suitable for artificial high-density cultivation. Clam shell is a significant by-product of aquaculture, where not being fully utilized beneficially, results in large numbers of discarded clam shells being accumulated. These discarded clam shells contain remnants of meat and other organic residuals, which will rot potentially producing toxins after long-term exposure to the environment, which has negative impact on aquaculture, and also causes serious environmental pollution. Therefore, mishandling of by-products from aquaculture has

previously led to environmental crisis due to the unwanted release of hazardous substances (Penarodriguez et al., 2010). Thus, an urgent waste issue to be resolved is how effectively and beneficially utilize waste clam shells. Previously oyster shells have been used to effectively adsorb H_2S from wastewater, with a maximum adsorption capacity of 12 mg g^{-1} (Asaoka et al., 2009). Through calcination and hydration, waste oyster shell has also been pretreated to increase its specific surface area and pore volume, for the removal of SO_2/NO_x (Jung et al., 2007). Oyster shell has also been used as an adsorption and filtration medium for phosphorus removal, where its use decreased eutrophication in wastewater (Park et al., 2008). have used Calcined mussel shells have been used to remove mercury (Hg) from water with good efficiency, reaching 90% in 55 min (Penarodriguez et al., 2010). A mixture of mussel shell calcined ash, sewage sludge and wood ash were used successfully as an adsorbent for several metal ions, with removal efficiencies for Hg, arsenic (As) and chromium (Cr) of is 98–99, 90–96, and 32%, respectively (Secoreigosa et al., 2014). Many different natural materials have also been used to specifically remove anthropogenic dyes. The residual biomass of *Spirulina platensis* removed up to 82.6% of CR (Nautiyal et al., 2016), while carbonized kelp biochar performed even better, removing up to 94% of MB (Zhou et al., 2018). These reports indicate that waste utilization of marine aquaculture by-products has been an important issue. Even today, increasing attention has been directed towards better methods for the utilization of marine aquaculture by-products, as many studies have stressed the importance and necessity of global waste utilization. Thus, there seems to be great potential for the

utilization of clam shell for cost-effective environmental pollution control. However, to the best of our knowledge, the potential for clam shell to act as a natural photocatalyst for dye degradation has not been previously studied, but this seems likely given the previous successes outlined above.

Thus, in this work, a natural photocatalyst based on calcium oxide derived from clam shell was synthesised via a high temperature calcination method and its physiochemical properties fully characterized by SEM, TEM, BET, XRD, XPS, UV-vis and TGA. Thereafter, the as-prepared photocatalysts were evaluated for their ability to adsorb and photocatalytically degrade both cationic (MB) and anionic (CR) dyes, where the mechanism of adsorption and photocatalytic degradation was explored.

2. Materials and Methods

2.1. Materials

Clam shells were collected from a local market in Zhoushan, Zhejiang Province. Methylene blue (MB), Congo red (CR), sodium hydroxide, hydrochloric acid, p-benzoquinone, isopropanol, hydrogen peroxide and ammonium oxalate were all purchased from Shanghai Guoyao Chemical Reagent Co., Ltd. All chemicals used in this work were analytical grade and were used directly as received without further purification.

2.2. Preparation of clam shell catalyst

Clam shells were initially washed with tap water to remove any obvious

158 contamination from the surface of the clam shell. Thereafter, clam shells were
159 immersed in a solution of 1 M sodium hydroxide and heated to 85 °C in a water bath
160 remove any residual meat from the surface of the clam shells, then, the samples were
161 rinsed with fresh water (pH = 7), and evaporated until dryness at 80 ° C on a stove.
162 The clam shells were soaked in 1 M hydrochloric acid solution in a clam pot
163 overnight, washed with deionized water several times and dried. Finally, the clam
164 shell was calcined in a muffle furnace for 2 h at 800, 900, and 1000 °C respectively.
165 After calcination, the white powder obtained was ground, sieved (100 mesh) and
166 stored in a desiccator for later use.

167 *2.3. Characterization*

168 Specific surface area and pore size distribution of samples, was calculated using
169 the BET method from N_2 adsorption/desorption isotherms obtained using a static
170 volumetric adsorption analyzer (Micromeritics ASAP 2010, Shanghai, China).
171 Morphology and microstructure of the as-prepared samples was determined via a
172 scanning electron microscope (SEM; S4800, Hitachi, Japan) and high-resolution
173 transmission electron microscope (HR-TEM; Joel-2100, JEOL, Japan). Crystal
174 structures were analyzed by X-ray diffraction (XRD, RIGAKU miniflex/600, Japan)
175 in the range between 20 ° – 80 °. Thermogravimetric analysis was conducted on a
176 TGA Q5000 (American TA instrument Q Series) to better understand phase
177 transformations during calcination. Optical properties of samples, were examined
178 using a Cary 500 UV-vis NIR spectrophotometer in the range 200 – 800 nm. The
179 chemical states of elements at the near surface of samples were also studied using X-

ray photoelectron spectroscopy (XPS, Phi 5000C ESCA system, USA).

2.4. Photocatalytic experiment

As-prepared photocatalyst (20 mg) was added into an aqueous solution of either MB or CR (40 mL) and the solution was magnetically stirred in the dark. for 2 hours for the reaction to achieve adsorption equilibrium. During this time aliquots of the supernatant solution were removed at regular intervals (i.e., 0, 5, 10, 20, 30, 60, 90 and 120 min) an analyzed for the residual dye concentration. To assess adsorption performance, residual dye concentration were determined photometrically.

After 2 h dark reaction, a light source (xenon lamp, HSX-F300) was used to initiate photocatalytic experiments. The vertical distance between the light source and the reactor was 10 cm, and supernatant samples were again taken at regularly intervals to assess photocatalytic performance. In the photocatalytic system, a cooling reflux device was also connected to the reaction vessel to eliminate the influence of heat generated by light on the experiment.

The effects of different dye concentrations (MB: 50, 75, and 100 ppm; CR: 400, 450, and 500 ppm), and different catalyst doses (20, 40, 60, and 80 mg) were also explored.

2.5. Determination of dye concentration

After the reaction single dye solution samples were initially centrifuged at 4000 r min^{-1} for 10 min, and the absorbance of the supernatant subsequently measured using an UV-vis spectrophotometer. The wavelengths of absorbance maxima for the two

dyes were λ_{MB}: 664, and λ_{CR}: 497 nm. The removal efficiency (R%) of adsorbed dye was calculated by Eq (1), where the amount of dye adsorbed on the catalyst q_e (mg/g) was calculated by Eq (2).

$$R(\%) = \frac{c_0 - c_e}{c_0} \times 100\% \quad (1)$$

$$q_e = \frac{(C_0 - C_e)V}{m} \quad (2)$$

$$-\ln(\frac{C_t}{C_0'}) = kt \quad (3)$$

where C_0 and C_e (mg L^{-1}) were respectively, the initial and equilibrium dye concentrations in solution, m (g) was the mass of cataclysm and V (L) was the volume of dye solution. In order to study reaction kinetics, the rate constant k was obtained by curve fitting data to Eq (3) t, where C'_0 is the initial dye concentration after dark reaction and C_t is the dye concentration at light irradiation time t.

2.6. Adsorption kinetics under dark reaction

Adsorption kinetics of the single dye system was further studied by adding catalyst to the dye solution under dark conditions with constant magnetic stirring and measuring the residual dye concentration in the solution at fixed time periods. The kinetic data so obtained was fit to both pseudo first order (PFO Eq 4) and second order (PSO Eq 5) kinetics to evaluate the kinetics of adsorption.

$$\ln(q_e - q_t) = \ln q_e - k_1 t \quad (4)$$

$$\frac{t}{q_t} = \frac{1}{k_2 q_e^{\,2}} + \frac{t}{q_e} \quad (5)$$

where q_t (mg g^{-1}) is the dye adsorption capacity at time (t); and k_1 (min^{-1}) and k_2 (g mg^{-1} min^{-1}) are the rate constants for PFO and PSO models, respectively.

3. Results and discussion

3.1. Characterization of catalyst

3.1.1. Morphology

The changes in clam shell powder morphology following calcination at three different temperatures were monitored using SEM and TEM (Fig. 1). Before calcination, clam shell powder had a spongy porous structure (Fig. a,b), due to presence of organic matter and a calcium carbonate skeleton after soaking in acid. However, after calcination at 800 °C, the clam shell surface became fragmented and bulky, due to the consumption of organic matter and growth of crystal particles (Fig. 1c,d). As calcination temperature further increased (900 and 1000 °C), clam shell powder morphology and surface structure became more compact. The increase in particle size was attributed particle sintering, resulting in Ostwald ripening, which causes growth of larger particles at the expense of smaller ones. This was consistent with previous results which had shown an increase in average surface grain size with calcination temperature (Peralta et al., 2017).

More detailed morphological characteristics of clam shell calcined at 1000 °C were obtained by HR-TEM (Fig. 1 i-k), and showed that after high temperature calcination the clam shell catalyst (CSC) had a layered structure where the distance between two adjacent lattices at the interface was 0.286 nm, which was consistent with XRD results (section 3.1.3) corresponding to the CaO (111) crystal face. In

addition, the observed heterojunctions between dislocations in the crystal structure may be due to the rearrangement of additional atomic layers produced by the presence of trace metals in the CSC during calcination (Wei et al., 2018). This may enable greater electron migration to the conductive band of CaO, since the energy band gap is reduced and charge carrier separation is increased, therefore improving photocatalytic performance.

< Insert Fig. 1 here >

3.1.2. BET analysis

All samples exhibited Type IV isotherms (Fig. S1 a and b) with hysteresis loops. The presence of small hysteresis loops at $P/P_0 > 0.4$ indicated the existence of both microporous and mesoporous structures (Yao et al., 2020). After calcination, specific surface area, pore volume and average pore diameter of the catalyst all decreased (Table S1). This was because as a result of an increase in calcination temperature, the inner part of the particles shrunk more, leading to an overall decrease in the pore size of the material. However, specific surface area of the catalyst did increase slightly between 800 and 1000°C, which was attributed to the formation of micro pores following decomposition of calcium carbonate. Adherence to the Type IV isotherm model clearly indicated the formation of multilayers on the catalyst surface during high temperature reactions, which was also clearly observed in TEM imagery (Fig 1 i).

3.1.3. X-ray diffraction analysis

268 The XRD patterns of samples calcined at different temperatures (Fig. 2a),
269 showed that the main component of untreated clam shell was $CaCO_3$, where
270 diffraction peaks at 2θ = 26.21°, 27.21°, 45.85° and 50.22° correspond to calcium
271 carbonate on (111), (021), (221) and (132) crystal faces, respectively (PDF 70-1849).
272 However, the XRD pattern of samples calcined at 800 °C for 2 h did not match well
273 with either $CaCO_3$ or CaO. This was because during heat treatment, calcium
274 carbonate, the main component of the clam shell, would have experienced major
275 structural changes from orthorhombic to trigonal-rhombohedral (Sree et al., 2020).
276 However, 800 ºC is not enough for complete conversion, so the calcined material
277 contains a large portion of intermediate phase/material between calcium carbonate and
278 calcium oxide. For samples calcined for 2 h at either 900 or 1000 °C the diffraction
279 peaks at 32.20°, 37.35°, 53.85°, 64.15° and 67.37° corresponded to calcium oxide on
280 (111), (200), (220), (311) and (222) crystallographic planes, respectively (Jiang et al.,
281 2018). In addition, closer comparison of the XRD patterns of the samples calcined at
282 900 °C and 1000 °C, showed that several small peaks present at 900 °C disappeared at
283 1000 °C. This was attributed to either further mass loss of trace metals or the
284 complete conversion of intermediate substance to CaO. During calcination, calcium
285 carbonate, the main component of clam shell, undergoes an initial phase change from
286 aragonite to calcite, and then subsequently from calcite to CaO.
287 < Insert Fig. 2 here >

288 *3.1.4. Thermogravimetric analysis*

289 Thermogravimetric analysis provides further information on the transformation

290 of clam shell powder during calcination. The initial mass lost from clam shell was
291 only 0.47% due to the loss of water between 30 - 200 °C (Fig. 2b). Thereafter, the
292 curve decreased slightly between 200 - 500 °C, due to the decomposition and removal
293 of organic components of the clam shell, whereas weight loss between 500 – 610 °C
294 was attributed to a phase transformation from aragonite to calcite. Thereafter, the
295 mass of clam shell decreased significantly between 610 and 800 °C, due to further
296 conversion of calcite to CaO and CO_2, during calcination (Shariffuddin et al., 2018).
297 At 800 - 900 °C, further mass loss was caused by removal of any residual
298 intermediate products from incomplete conversion of $CaCO_3$ to CaO, and thereafter
299 the slight decrease observed at 900 - 1000 °C, may be due to the presence of a small
300 amount of unconverted $CaCO_3$ and further mass loss of trace metals. All these results
301 were in good agreement with both XRD (Section 3.1.3) and XPS (Section 3.1.6)
302 analysis.
303
304 *3.1.5. Ultraviolet visible spectrum analysis*
305 Diffuse reflectance spectroscopy in the UV-vis range was employed to
306 investigate the optical properties of uncalcined clam shell powder and clam shell
307 calcined at three different temperatures (Fig. 2c), as well as the light absorption
308 characteristics and band gap energy of the CSCs (Fig. 2d). The wavelength absorption
309 maxima of uncalcinated, 800, 900 and 1000 °C samples were 277, 271, 276 and 273
310 nm, respectively (Fig. 2c), corresponding to the optical band gap obtained from Tauc
311 diagram (Fig. 2d). It was found that the optical band gap of the catalysts decreased

312 with an increase in calcination temperature, and thus the lowest band gap (2.64 eV)
313 was obtained at 1000 °C. As the calcination temperature increased, the weight of clam
314 shell decreased, and the specific gravity of trace metal elements increased. Therefore,
315 the decrease in optical band gap with increased calcination temperature was attributed
316 to the appearance of localised energy states in the CaO band gap and the existence of
317 a higher content of lattice defects, i.e., increases in trace metals and oxygen vacancies
318 (Shajahan et al., 2020). High resolution TEM (Section 3.1.1) had also confirmed the
319 existence of a large number of lattice defects.
320
321 *3.1.6. XPS analysis*
322 In order to analyze the valence state and content of surface elements in clam
323 shell powder before and after high temperature (1000 °C) calcination, XPS was
324 performed and compared on clam shell treated at 800 and 1000 °C (Fig, 3). Survey
325 scans (Fig. 3a), indicated that the main components of clam shells at 800 and 1000 °C
326 were C, O, Ca and a small amount of Na. It is likely that traces of other metals such as
327 magnesium (Mg) are also present but these would be at levels below the detection
328 limit of XPS (i.e., < 0.01 %).
329 For clam shell powder calcined at 800 °C, the XPS spectra (Fig. 3b) exhibited
330 many superimposed C1s peaks (C1-C3), where C1 with a binding energy of 285 eV,
331 was attributed to amorphous carbon/adventitious carbon, a small standard C2 peak at
332 286.1 eV, corresponded to the C-O, and the C3 peak at 289.4 eV corresponded to a
333 binding energy commonly associated with metal carbonate MCO_3, and was thus

attributed to $CaCO_3$. In comparison, for clam shell calcined at 1000 °C (Fig. 3e), the binding energy of the adventitious carbon peak C1 occurred at 285 eV, the C2 peak for organic carbon (C-O bond) occurred at 286 eV, the C3 peak attributable to COOR at 288 eV, and the C4 peak corresponding to MCO_3 at 289.4 eV. However, compared with the sample calcined at 800 °C, the sample calcined at 1000 °C, exhibited two extra weak peaks (C5 and C6) at 292 and 295 eV, respectively, which were attributed to compounds formed by carbon and/or halogen. The observed peak (O1) at 530.8 eV for the 800 °C calcined sample in the O1s XPS spectra was attributed to CO_3^{2-} of $CaCO_3$ (Fig. 3c); whereas the binding energy of the peak at 531.6 eV (peak O2) for the clam shell calcined at 1000 °C (Fig. 3f). corresponded to CaO.

Calcium typically exhibits two characteristic binding energies, i.e., $Ca2p_{3/2}$ (346 eV) and $Ca2p_{1/2}$ (349.6 eV) (Tangboriboon et al., 2012). Here high-energy resolution spectra of Ca2p peaks showed a complex pattern that could be deconvoluted into three (Ca1, CA2 and Ca3) constituent peaks (Fig. 3d and g). For sample calcined at 800 °C, peak Ca1 (346 eV), corresponding to $CaCO_3$ and peak Ca2 (347.1 eV) was associated with CaO. In comparison, for the 1000 °C calcined sample the area of the CaO peak (Ca2) increased, indicating that the content of CaO was relatively more when the sample was pyrolyzed at the higher temperature.

< Insert Fig. 3 here >

3.2. Adsorption-photodegradation performance

3.2.1. Effect of different catalysts

While the total adsorption-photodegradation removal efficiency of MB and CR for calcined clam shells at 1000 °C reached 99.7 and 90.8%, respectively, under dark conditions, the adsorption only removal efficiencies of MB and CR reached only 25.9 and 70.5%, respectively (Fig. 4). In comparison the total absorption-photodegradation removal efficiency of untreated clam shells (MB: 15.9%, CR: 10.4%), and those calcined at 800 °C (MB: 53.9%, CR: 25.9%), or 900 °C, (MB: 85.7%, CR: 81.1%) was lower. This indicated that the adsorption and/or photocatalytic properties of uncalcined clam shell or clam shell calcined at temperatures < 1000 ºC were poorer than clam shell calcined at 1000 °C. It can also be clearly seen (Fig. 4) that the adsorption performance (dark environment) of clam shell calcined at different temperatures was consistently better than that of non-calcined clam shell. This suggested that decomposition of residual organic matter in the original clam shell via heat treatment during calcination, results in significantly more pore structure. Where the increase in adsorption performance with calcination temperature, could be attributed to increased pore forming effects from CO_2 generated by thermal decomposition of $CaCO_3$, the main component of clam shell. The photocatalytic activity (under light) of the clam shell powder was also enhanced by an increased calcination temperature. This may be due to an increase in the relative content of calcium oxide due to heating and the interaction of trace transition metals in the clam shell. HR-TEM images confirmed the presences of a significant number of dislocations and defects in the CaO crystal structure. Overall, the results from the adsorption-photodegradation study indicated that the best photocatalytic performance

was obtained when clam shell powder was calcined at 1000 °C. This was attributed to synergetic effects of enhanced absorption and increased heterojunctions among some dislocations in the crystal structures, which also improved photodegradation efficiency.

Photodegradation kinetics of both MB and CR by CSCs varied with the calcination temperature of the catalyst (Fig. 4b and d). The kinetic data for the degradation of both MB and CR best fit the pseudo first order kinetic model (R^2 approaching 1), where the rate constant (k) increased with calcination temperature (Table 1), and the higher the k value, the better the photocatalytic performance and the greater the photodegradation amount. Thus, in all subsequent experiments, only clam shell calcined at 1000 °C were investigated.

The photodegradation of both MB and CR by 1000 °C calcined CSC occurs in the visible light region of the absorption spectrum (Fig. 4e and f). As reaction time increased, peaks of MB and CR both decreased sharply, and some peaks disappeared or were slightly shifted in wavelength, which indicated that both MB and CR molecules were being destroyed, and that new substances (degradation products) were also formed (Shariffuddin et al., 2018).

< Insert Fig. 4 here >

< Insert Table 1 here >

3.2.2. *Adsorption performances*

The adsorption performance of 1000 °C calcined clam shell powder varied with

400 the initial concentrations of MB and CR within 2 h. (Fig. S2) Over 2 h the
401 concentration of both MB or CR decreased gradually after exposure to the CSC until
402 the adsorption equilibrium was reached. When the initial dye concentration was low,
403 equilibrium was reached relatively quickly, within 30 min). For example, for MB a
404 sharp decrease in MB concentration was observed in the first 10 min followed by a
405 slower adsorption until the MB concentration stabilized. This is because when the
406 initial dye concentration is low, the adsorption reaction can quickly reach equilibrium
407 because there are a large number of sites available on the surface of CSC for
408 adsorption relative to the number of MB molecules. As the initial concentration of dye
409 increases, a more competitive adsorption for MB molecules for surface sites is
410 induced. Thus, as more active sites become occupied, it becomes increasingly more
411 difficult to adsorb dye due to a weaker attraction between the surface of CSC and the
412 MB molecules, which leads to slowing of dye adsorption rate in the latter stages of the
413 reaction.

414 In order to further investigate the adsorption mechanism of the MB dye on to the
415 CSC, both pseudo first order (PFO) (Eq 4) and pseudo second order (PSO) (Eq 5)
416 kinetic models were used for data analysis. The kinetic data for MB adsorption on to
417 CSC fit both the PFO (Fig S2(c)) and PSO (Fig. S2(d)) models well with good linear
418 behavior. However, the goodness of fit (R^2) for the PSO model was slightly higher
419 than that for the PFO model, and the adsorption capacity at equilibrium obtained from
420 PSO fitting was also closer to the experimental value (Table S2). The corresponding
421 adsorption capacities for initial MB concentrations of 50, 75 and 100 ppm were

422 experimentally is 60.52, 96.72 and 123.45 mg g^{-1}, respectively. Therefore, the PSO
423 model was more suitable for describing the adsorption system operating for the CSC.
424 Based on the underlying assumptions of the PSO equation model this indicates that
425 MB participated in chemical adsorption, involving the sharing or exchange of
426 electrons between the hydrophilic edge sites of the CSC and the dye cations
427 (Hosseinzadeh et al., 2015). As the initial MB concentration increased, the goodness
428 of fit of adsorption capacity (q_e) also increased, and became very close to the
429 experimentally derived q_e value, but the adsorption rate (k_2 value) decreased. This
430 decrease in rate constant is due to the intense adsorption competition between
431 relatively limited surface-active sites and a large number of MB molecules in a higher
432 concentration dye solution, resulting in a relatively low-rate constant (Liu et al.,
433 2014).

434 Similarly, the initial adsorption capacities of CR at 400, 455 and 500 ppm were
435 592.76, 653.26 and 679.91 mg g^{-1}, respectively and fitting of the kinetic data to the
436 same two models (Fig. S2 (g) and (h)) showed that the PSO model better described
437 the adsorption system of CR on the CSC, and calculated adsorption amount at
438 equilibrium was also closer to the experimental value (Table S2). As for MB, since the
439 PSO model assumes chemical adsorption as the dominant adsorption process
440 (Ardejani et al., 2008; Parvin et al., 2019), which involves the sharing or exchange of
441 electrons between the hydrophilic edge sites of the CSC and the dye ions, this result
442 also suggests that negatively charged CR ions were removed from solution via a
443 chemical adsorption process. This adsorption may be caused by a combination of π-π

444 stacking, hydrogen bonding, and van der Waals forces. In addition, the k_1 values for
445 CR were much lower than those calculated for MB, which indicated that the CSC had
446 a higher affinity for the negatively charged dye (Dai et al., 2018).
447 *3.2.3. Effect of catalyst dose*
448 The dose of catalyst is an important practical consideration and also plays an
449 important role in the efficiency of photocatalytic reaction. An increase in catalyst dose
450 will increase the overall concentration of active substance and hence increase the
451 number of active sites in the reaction system. Thus, the probability of contact of dye
452 molecules with the active sites increases, as does the reaction probability, and rate of
453 reaction, leading to improved dye removal efficiency. For photodegradation removal
454 processes there will generally be an increase in removal efficiency with increased
455 dose until at a certain concentration the increase in catalyst amount reduces the light
456 transmittance of the suspension (Nguyen et al., 2018) and hence the removal
457 efficiency.
458 For MB and CR (Fig. 5) as the amount of CSC increased from 20, 40, 60 to 80
459 mg, the removal efficiencies of MB were 99.7, 99.8, 99.9 and 99.9%, respectively,
460 and 83.3, 88.6, 96.7% and 97.0% for CR, respectively. Thus, for both dyes' removal
461 efficiency increases with catalyst dose, being almost a negligible for MB and only
462 modest for CR. This indicated that even the lowest dose used here had an adsorption
463 capacity well above the amount of dye in solution. Even though the increase in MB
464 removal efficiency with dose was not very significant, the time required to achieve
465 this removal became less as dose increased (Fig. 5b). Since even a 20 mg catalyst

dose could achieve a strong catalytic effect, in 40 mL dye solutions a catalyst dose of 0.5 g L^{-1} was selected for all subsequent experiments. According to the experimental data, enough binding sites can be reached at 20 mg. Although the removal efficiency further increases with the increase of the amount of catalyst, it will cause the waste of catalyst, that is, some more binding sites are not used.

< Insert Fig. 5 here >

< Insert Table 2 here >

The best fit kinetic parameters (Table 2) for MB and CR degradation under different catalyst doses showed that the degradation of both MB and CR followed pseudo first order kinetics, with good correlation (R^2 close to 1).

The k value for MB increased slightly in the range of 20 - 40 mg, and decreased between 40 and 80 mg. This was potentially because the increase of catalyst above 40 mg reduced the light transmittance of the suspension, making it more difficult for photons to reach the CSC surface, and the amount of •OH free radical formed between dye molecules and catalyst surface became relatively small. However, for CR, the k value increased significantly between 20 and 60 mg, and slightly increased from 60 to 80 mg.

3.2.4. Effect of initial dye concentration

The removal efficiencies of MB dye at initial dye concentration of 50, 75 and 100 ppm were 99.8%, 99.7% and 99.6%, respectively (Fig. 6). Although the removal efficiency did not significantly change with initial dye concentration, the time required for the photodegradation become longer (Fig. 6). Likewise, after 120 min of

illumination, the overall removal efficiency of CR dye decreased with an increase in the initial dye concentration, being 98.2, 90.8 and 83.3%, for CR concentration of 400, 450 and 500 ppm respectively. This is because the number of •OH radicals formed on the catalyst surface and the number of interactions with dye molecules determine the overall efficiency of photocatalytic degradation. With an increase in the number of dye molecules in solution, the number of dye molecules contacting the catalyst surface also increase, causing active sites on the catalyst surface covered by them, these will affect the arrival of photons on the surface of the catalyst, which will reduce the catalytic efficiency, resulting in less •OH radical generation on the catalyst surface. Therefore, increased dye concentration can lead to a reduction in both degradation efficiency and reaction rate (Zhu et al., 2000).

The variation in best fit degradation kinetic parameters for both MB and CR with different concentrations are shown in Table 3. The k values of both MB and CR increased as the initial dye concentration decreased. The maximum k value of 0.058 min^{-1} was observed for MB, which demonstrated that this catalyst had the highest photocatalytic degradation rate for MB. This was also much higher than result obtained using other semiconductors such as TiO_2/MoS_2 with k = 0.040 min^{-1} (Ibukun et al., 2019), g-C_3N_4/MnV_2O_6 (1:1), k = 0.022 min^{-1} (Nithya et al., 2019); $CaTiO_3$:0.5%Eu^{3+}, k = 0.005 min^{-1} (Chen et al., 2020b); and Bi_2CrO_6, k = 0.006 min^{-1} (Li et al., 2020).

< Insert Fig. 6 here >

< Insert Table 3 here >

3.2.5. Influence of free radical scavengers on catalyst performance

Since the photodegradation efficiency of the catalyst is likely to depend on the concentration of free radicals at the surface, free radical scavengers can affect photodegradation performance. Here, in order to examine the factors affecting the performance of the catalyst, isopropanol (IP) as •OH radical scavenger, p-benzoquinone (BQ) as an $\bullet O_2^-$ radical scavenger and ammonium oxalate (AO) as h^+ scavenger were added to the reaction system (Wen et al., 2016; Chen et al., 2020a). Under illumination from a xenon lamp, the removal efficiencies of MB with BQ, AO and IP were 88.6%, 93.9% and 95.0%, respectively (Fig. 7) compared to a MB removal efficiency of 99.9 with no added scavengers Similarly, the removal efficiencies for CR after adding BQ, AO and IP were 64.9, 83.5 and 88.4% respectively, compared to 90.8% without any added scavenger.

The presence of BQ, significantly inhibited the removal efficiencies of both MB and CR This was because BQ leads a decrease in the amount of superoxide radicals present, which leads to a significant decrease in the photodegradation rate (Table 4). in comparison, AO and IP induced only slight decreases in the removal efficiencies of MB and CR. These experimental results imply the while the formation of $\bullet O_2^-$ and h^+ in the photocatalytic reaction are both essential for a high removal efficiency, $\bullet O_2^-$ is the dominant reactive species in this reaction.

These observations allow a removal mechanism to be proposed. When the CSC is irradiated by a xenon lamp, h^+ electron holes are generated in the collision gap. Oxygen molecules in the mixed solution form $\bullet O_2^-$ superoxide radicals by electron

532 removal, and holes (h^+) react with water to form •OH radical (Baliarsingh et al.,
533 2014).

534 < Insert Fig. 7 here >

535 < Insert Table 4 here >

536 The addition of hydrogen peroxide (H_2O_2) is often used as an amendment to
537 enhance photocatalytic degradation of organic materials by enhancing free radical
538 generation. Here, under H_2O_2 assisted photocatalysis, the removal efficiencies of MB
539 and CR were 99.9% and 97.1%, respectively, indicating that compared to the blank
540 samples (99.6% and 90.8%), the addition of H_2O_2 significantly improved the
541 photodegradation removal efficiency. The reaction rate constants of the two dyes were
542 also close to each other, indicating that these two dyes were removed via similar
543 mechanisms.

544 H_2O_2 assisted photocatalysis works through the formation of hydrogen peroxide
545 ion (HO_2^-) via reaction with H_2O, accelerating the hydrolysis of H_2O_2 forming OH
546 radical, and is accompanied by the formation of hydrogen hydrate ion (H_3O^+)
547 (Kausley et al., 2017), and the further reaction of HO_2^- and H_2O_2 forms OH radical,
548 which is the decisive step of the degradation rate of organic pollutants in aqueous
549 solution (Li et al., 2018). The reaction mechanism is summarized as follows:

550 $$H_2O_2 + H_2O \longrightarrow H_2O^- + H_3O^+ \quad (6)$$

551 $$H_2O_2 + HO_2^- \longrightarrow OH\cdot + HO_2\cdot + OH^- \quad (7)$$

552

553 In the process of photocatalytic degradation of dyes, the electrons generated by
554 the catalyst can react with O_2 to form $\bullet O_2^-$, and then the products can react with water

555 to form hydrogenated oxygen radicals ($HO_2\bullet$) and hydroxyl radicals (OH^-). The
556 generated $HO_2\bullet$ rearranges to form oxygen (O_2) and peroxide hydrogen (H_2O_2)
557 (Kumar et al., 2015), and H_2O_2 reacts with superoxide radical to form hydroxyl
558 radical (OH^-). The generated hole (h^+) interacts with water to form a highly reactive
559 hydroxyl radical, the hole itself can also attack dye molecules to produce by-products
560 as well. After the formation of free radicals, the reactive substance ($\bullet O_2^-$) attacks dye
561 molecules until the end of decolourisation and ring opening reaction, effectively
562 degrading the dye into smaller intermediates and the final products (CO_2 and H_2O)
563 (Kaviyarasu et al., 2017; Magdalane et al., 2016; Chen et al., 2008). The possible
564 photocatalytic reactions are as follows:

565 $$CaO + hv \longrightarrow h^+ + e^- \quad (8)$$

566 $$e^- + O_2 \longrightarrow \cdot O_2^- \quad (9)$$

567 $$\cdot O_2^- + H_2O \longrightarrow OH^- + HO_2\cdot \quad (10)$$

568 $$2HO_2\cdot \longrightarrow O_2 + H_2O_2 \quad (11)$$

569 $$H_2O_2 + \cdot O_2^- \longrightarrow O_2 + OH^- + \cdot OH \quad (12)$$

570 $$h^+ + H_2O \longrightarrow \cdot OH + H^+ \quad (13)$$

571 $$Dye + hv \longrightarrow Dye^* \quad (14)$$

572 $$Dye^* + (\cdot OH, \cdot O_2^-, h^+) \longrightarrow Intermediates \longrightarrow CO_2 + H_2O \quad (15)$$

573

574 *3.3. Proposed photocatalytic mechanism*

575 Based on the above experimental studies, a possible mechanism for the
576 photocatalytic degradation of dyes by the CSC produced here was proposed (Fig S3).
577 Under light irradiation, the electrons gain sufficient energy to become excited and

578 transition from the valence band to the conduction band, and form excitons (electron-
579 hole pairs). These excitons are known to act in four potential ways: (1) intralattice
580 recombination, (2) recombination at surface active sites, (3) hole (h^+) oxidizes
581 external dyes, and (4) electron (e^-) reduces external dyes. High photocatalytic activity
582 can be achieved through the minimum photocatalytic system of electron hole
583 recombination, and the combination of effective absorption and enhanced electron
584 transition from heterojunctions among some dislocations in the crystal structures (Xu
585 et al., 2018; Park et al., 2014). It was previously reported that photocatalytic
586 degradation efficiency can also be further improved via effective size reduction of
587 CaO nanoparticles and the innate nano properties of the initial raw materials
588 (Anantharaman et al., 2016). Hence, calcium oxide nanoparticles synthesized by
589 calcination of marine biomass, such as shells or other biomass materials containing
590 metal oxides and trace transition metals, which can act as excellent natural
591 photocatalysts for the degradation of dyes from the textile industries. In contrast,
592 while the photodegradation efficiency of 50 mg CaO derived from eggshell biomass
593 catalyst can reach 96.2% at an initial MB dye concentration of 20 mg L^{-1} through
594 parameter optimization (Sree et al, 2020), here, the photodegradation efficiency using
595 a 20 mg CSC derived from marine biomass reached 99.6% for an initial MB dye
596 solution concentration of 100 mg L^{-1}.

597 *3.4. Feasibility of practical application*

598 In the textile industry, dye wastewater typically contains many kinds of different
599 dyes which need to be simultaneously removed. Hence here, the feasibility of

applying a CSC for practical wastewater treatment was evaluated in a mixed dye solution. The results indicated that 20 mg of CSC could easily degrade both a mixed dark colored binary dye solution (100 ppm MB + 100 ppm CR) and a ternary dye system (75 ppm MB + 75 ppm CR + 75 ppm rhodamine B (Rh B)) into a transparent solution (Fig S4). Analysis of the absorption spectra of the mixed dye solution system under visible-light irradiation, showed that the initial peaks of the mixed dye solution decreased sharply as reaction time increases, with some peaks shifting slightly or completely disappearing, which strongly suggested that mixtures of dye molecules were destroyed or degraded, and new substances were formed.

4. Conclusion

A novel photocatalyst nanomaterial derived from natural clam shell was successfully prepared via a facile calcination process. The as prepared material was then evaluated for its potential to treat dye contaminated wastewater. Under xenon lamp illumination, the overall absorbance- photocatalytic removal efficiencies for 100 mg L^{-1} MB and 500 mg L^{-1} CR reached 99.6 and 83.3 %, respectively. Increasing the calcination temperature enhanced the catalytic performance of the catalyst. This was attributed to synergetic effects of increased absorption together with increased heterojunctions among some dislocations in the crystal structures. Increased numbers of heterojunction can greatly reduce the energy required for electron transition, making it much easier to form holes and excited electrons. Consequently, the inexpensive clam shell photocatalyst, synthesized in this work from a marine biowaste, may have great potential for future practical large-scale industrial

wastewater treatment applications.

Declaration of Competing Interest

The authors declare that they have no known competing financial interests or personal relationships that could have appeared to influence the work reported in this paper.

Acknowledgments

This work is supported by the National Key Research and Development Projects of China (No. 2020YFE0200100, 2019YFD0900904). We also gratefully acknowledge the funding support from the Fundamental Research Funds for Zhejiang Provincial Universities and Research Institutes (No. 2019J00045) which has made this work possible, as well as the Bureau of Science and Technology of Zhoushan (No: 2018C21020).

References

1. Aboutaleb, W.A., Elsalamony, R.A., 2019. Effect of Fe_2O_3-CeO_2 nanocomposite synthesis method on the Congo red dye photodegradation under visible light irradiation. Mater Chem Phys, 236, 121724

2. Anantharaman, A., Ramalakshmi, S., George, M., 2016. Green Synthesis of Calcium Oxide Nanoparticles and Its Applications. Int J Eng Res Appl. 6, 27-31.

3. Ardejani, F.D., Badii, K., Limaee, N.Y., Shafaei, S.Z., Mirhabibi, A.R., 2008. Adsorption of Direct Red 80 dye from aqueous solution onto almond shells: effect of pH, initial concentration and shell type. J Hazard Mater, 151, 730-737.

4. Asaoka, S., Yamamoto, T., Kondo, S., Hayakawa, S., 2009. Removal of hydrogen sulfide using crushed oyster shell from pore water to remediate

649 organically enriched coastal marine sediments, Bioresource Technol. 100, 4127-
650 4132.

651 5. Balakrishnan, V.K., Shirin, S., Aman, A., Solla, S.R., Mathieudenoncourt, J.,
652 Langlois, V. S., 2016. Genotoxic and carcinogenic products arising from
653 reductive transformations of the azo dye, Disperse Yellow 7. Chemosphere, 146,
654 206-215.

655 6. Baliarsingh, N., Parida, K.M., Pradhan, G.C., 2014. Effects of Co, Ni, Cu, and Zn
656 on Photophysical and Photocatalytic Properties of Carbonate Intercalated MII/Cr
657 LDHs for Enhanced Photodegradation of Methyl Orange. Ind Eng Chem Res, 53,
658 3834-3841.

659 7. Chen, J., Luo, W., Yu, S., Yang, X., Wu, Z., Zhang, H., Gao, J., Mai, Y., Li, Y.,
660 Jia, Y., 2020a. Synergistic effect of photocatalysis and pyrocatalysis of
661 pyroelectric $ZnSnO_3$ nanoparticles for dye degradation. Ceram Int, 46, 9786-
662 9793.

663 8. Chen, J., Sheng, Y., Song, Y., Chang, M., Zhang, X., Cui, L., Meng, D., Zhu, H.,
664 Shi, Z., Zou, H., 2018. Multimorphology mesoporous silica nanoparticles for dye
665 adsorption and multicolor luminescence applications. ACS Sustain Chem Eng, 6,
666 3533-3545.

667 9. Chen, M., Xiong, Q., Liu, Z., Qiu, K., Xiao, X., 2020b. Synthesis and
668 photocatalytic activity of Na^+ co-doped $CaTiO_3$:Eu^{3+} photocatalysts for
669 methylene blue degradation. Ceram Int, 46, 12111-12119.

670 10. Chen, T., Zheng, Y., Lin, J. M., Chen, G., 2008. Study on the
671 photocatalyticdegradation of methyl orange in water using Ag/ZnO as catalyst by

672 liquid chromatography electrospray ionization ion-trap mass spectrometry. J Am
673 Soc Mass Spectr, 19, 997-1003.

674 11. Chequer, F.M., Angeli, J.P., Ferraz, E.R., Tsuboy, M.S., Marcarini, J.C.,
675 Mantovani, M.S., Oliveira, D.P., 2009. The azo dyes Disperse Red 1 and
676 Disperse Orange 1 increase the micronuclei frequencies in human lymphocytes
677 and in HepG2 cells. Mutat Res-Gen Tox En, 676 (1), 83-86.

678 12. Dai, L., Zhu, W., He, L., Tan, F., Zhu, N., Zhou, Q., He, M., Hu, G., 2018.
679 Calcium-rich biochar from crab shell: An unexpected super adsorbent for dye
680 removal. Bioresource Technol, 267, 510-516.

681 13. Hosseinzadeh, H., Mohammadi, S., 2015. Quince seed mucilage magnetic
682 nanocomposites as novel bioadsorbents for efficient removal of cationic dyes
683 from aqueous solutions. Carbohyd Polym, 134, 213-221.

684 14. Ibukun, O., Evans, P.E., Dowben, P.A., Jeong, H.K., 2019. Titanium dioxide-
685 molybdenum disulfide for photocatalytic degradation of methylene blue. Chem
686 Phys, 525, 110419.

687 15. Ismail, M., Wu, Z., Zhang, L., Ma, J., Jia, Y., Hu, Y., Wang, Y., 2019. High-
688 efficient synergy of piezocatalysis and photocatalysis in bismuth oxychloride
689 nanomaterial for dye decomposition. Chemosphere, 228, 212-218.

690 16. Jiang, D., Cai, L., Ji, L., Zhang, H., Song, W., 2018. Nano-Bi2MoO6/calcined
691 mussel shell composites with enhanced photocatalytic performance under visible-
692 light irradiation. Micro Nano Lett, 13, 1021-1025.

693 17. Jung, J., Yoo, K., Kim, H. G., Lee, H.K., Shon, B., 2007. Reuse of Waste Oyster
694 Shells as a SO_2/NO_x Removal Absorbent. J Ind and Eng Chem, 13, 512-517.

18. Kausley, S., Desai, K.S., Shrivastava, S., Shah, P.R., Patil, B.R., Pandit, A.B., 2017. Mineralization of alkyd resin wastewater: Feasibility of different advanced oxidation processes. J Environ Chem Eng, 6, 3690-3701.

19. Kaviyarasu, K., Kotsedi, L., Simo, A., Fuku, X., Mole, G. T., Kennedy, J., Maaza, M., 2017. Photocatalytic activity of ZrO_2 doped lead dioxide nanocomposites: Investigation of structural and optical microscopy of RhB organic dye. Appl Surf Sci, 421, 234-239.

20. Kumar, R., Umar, A., Kumar, G., Akhtar, M.S., Wang, Y., Kim, S.H., 2015. Ce-doped ZnO nanoparticles for efficient photocatalytic degradation of direct red-23 dye. Ceram Int, 41, 7773-7782.

21. Li, Y., Li, L., Chen, Z., Zhang, J., Gong, L., Wang, Y., Zhao, H., Mu, Y., 2018. Carbonate-activated hydrogen peroxide oxidation process for azo dye decolorization: Process, kinetics, and mechanisms. Chemosphere, 192, 372-378.

22. Li, Z., Zhang, Z., Wang, L., Meng, X., 2020. Bismuth chromate (Bi_2CrO_6): A promising semiconductor in photocatalysis. J Catal, 382, 40-48.

23. Liu, R., Liu, Y., Zhu, X., Zhang, Z., Zhang, J., Dang, F., 2014. Biomass-derived highly porous functional carbon fabricated by using a free-standing template for efficient removal of methylene blue. Bioresource Technol, 154, 138-147.

24. Ma, C., Wang, F., Zhang, C., Yu, Z., Wei, J., Yang, Z., Li, Y., Li, Z., Zhu, M., Shen, L., Zeng, G., 2017. Photocatalytic decomposition of Congo red under visible light irradiation using MgZnCr-TiO_2 layered double hydroxide. Chemosphere, 168, 80-90.

25. Magdalane, C.M., Kaviyarasu, K., Vijaya, J.J., Siddhardha, B., Jeyaraj, B., 2016. Photocatalytic activity of binary metal oxide nanocomposites of CeO_2/CdO nanospheres: Investigation of optical and antimicrobial activity. J Photoch Photobio B, 163, 77-86.

26. Nautiyal, P., Subramanian, K.A., Dastidar, M.G., 2016. Adsorptive removal of dye using biochar derived from residual algae after in-situ transesterification: Alternate use of waste of biodiesel industry. J Environ. Manage, 182, 187–197.

27. Nguyen, C. H., Fu, C., Juang, R., 2018. Degradation of methylene blue and methyl orange by palladium-doped TiO_2 photocatalysis for water reuse: Efficiency and degradation pathways. J Clean Prod, 202, 413-427.

28. Nithya, M., Vidhya, S., Keerthi., 2019. A Novel g-C_3N_4/MnV_2O_6 Heterojunction Photocatalyst for the Removal of Methylene Blue and Indigo Carmine. Chem Phys Lett, 737, 136832.

29. Park, S., Lee, C.W., Kang, M.G., Kim, S., Kim, J.H., Kwon, J.E., Park, S.Y., Kang, C., Hong, K.S., Nam, K., 2014. A ferroelectric photocatalyst for enhancing hydrogen evolution: polarized particulate suspension. Phys Chem Chem Phys, 16, 10408-10413.

30. Park, W. H., Polprasert, C., 2008. Roles of oyster shells in an integrated constructed wetland system designed for P removal. Ecol Eng, 34, 50-56.

31. Parvin, S., Biswas, B.K., Rahman, A., Rahman, H., Anik, S., Uddin, R., 2019. Study on adsorption of Congo red onto chemically modified egg shell membrane. Chemosphere, 236, 124326.

739 32. Penarodriguez, S., Fernandezcalvino, D., Novoamunoz, J.C., Ariasestevez, M.,
740 Nunezdelgado, A., Fernandezsanjurjo, M.J., Alvarezrodriguez, E., 2010. Kinetics
741 of Hg(II) adsorption and desorption in calcined mussel shells. J Hazard Mater,
742 180, 622-627.

743 33. Peralta, M.D., Sanchezcantu, M., Puentelopez, E., Rubiorosas, E., Tzompantzi,
744 F., 2017. Evaluation of calcium oxide in Rhodamine 6G photodegradation. Catal
745 Today, 305, 75-81.

746 34. Secoreigosa, N., Cutillasbarreiro, L., Novoamunoz, J. C., Ariasestevez, M.,
747 Fernandezsanjurjo, M. J., Alvarezrodriguez, E., Nunezdelgado, A., 2014.
748 Mixtures including wastes from the mussel shell processing industry: retention of
749 arsenic, chromium and mercury. J Clean Prod, 84, 680-690.

750 35. Shajahan, S., Arumugam, P., Rajendran, R., Munusamy, A.P., 2020.
751 Optimization and detailed stability study on Pb doped ceria nanocubes for
752 enhanced photodegradation of several anionic and cationic organic pollutants.
753 Arab J Chem, 13, 1309-1322.

754 36. Shariffuddin, J.H., Yean, W.C., Ghazali, S.S., 2018. Investigating the catalytic
755 properties of calcium compounds derived from marine based shell waste for
756 wastewater treatment, Materials Today Proceed. 5, 21718–21727.

757 37. Sree, G.V., Nagaraaj, P., Kalanidhi, K., Aswathy, C.A., Rajasekaran, P., 2020.
758 Calcium oxide a sustainable photocatalyst derived from eggshell for efficient
759 photodegradation of organic pollutants, J Clean Prod. 270, 122294-122302.

760 38. Tangboriboon, N., Kunanuruksapong, R., Sirivat, A., 2012. Preparation and
761 properties of calcium oxide from eggshells via calcination. Mater Sci-poland, 30,
762 313-322.

763 39. Tsai, C., Tseng, W.J., 2020. Preparation of TiN–TiO_2 composite nanoparticles for
764 organic dye adsorption and photocatalysis. Ceram Int, 46, 14529-14535.

765 40. Wei, D., Zhang, H., Cai, L., Guo, J., Wang, Y., Ji, L., Song, W., 2018. Calcined
766 Mussel Shell Powder (CMSP) via Modification with Surfactants: Application for
767 Antistatic Oil-Removal. Materials, 11, 1410.

768 41. Wen, X., Zhang, C., Niu, C., Zhang, L., Huang, D., Wang, X., Zhang, X., Zeng,
769 G., 2016. Facile synthesis of a visible light α-Fe2O3/BiOBr composite with high
770 photocatalytic performance. RSC Adv, 6, 4035-4042.

771 42. Xu, X., Wu, Z., Xiao, L., Jia, Y., Ma, J., Wang, F., Wang, L., Wang, M., Huang,
772 H., 2018. Strong piezo-electro-chemical effect of piezoelectric BaTiO3
773 nanofibers for vibration-catalysis. J Alloy Compd, 762, 915-921.

774 43. Yao, X., Ji, L., Guo, J., Ge, S., Lu, W., Cai, L., Wang, Y., Song, W., Zhang, H.,
775 2020. Magnetic activated biochar nanocomposites derived from wakame and its
776 application in methylene blue adsorption. Bioresource Technol, 302, 122842.

777 44. Zhou, Y., Zhang, H., Cai, L., Guo, J., Wang, Y., Ji, L., Song, W., 2018.
778 Preparation and characterization of macroalgae biochar nanomaterials with highly
779 efficient adsorption and photodegradation Ability. Materials, 11, 1709-1718.

780 **45.** Zhu, C., Wang, L., Kong, L., Yang, X., Wang, L., Zheng, S., Chen, F., Maizhi,
781 F., Zong, H., 2000. Photocatalytic degradation of AZO dyes by supported TiO2 +
782 UV in aqueous solution. Chemosphere, 41, 303-309.

Figure captions:

Figure 1. SEM images of clam shell samples: (a), (b) uncalcined; (c), (d) treated at 800 °C; (e), (f) treated at 900 °C; (g), (h) treated at 1000 °C; and TEM image (i), (j) and (k) treated at 1000 °C.

Figure 2. (a) XRD spectra of uncalcined, treated at 800, 900, and 1000 °C clam shell samples. (b) Thermogravimetric analysis of clam shell during calcination process. (c) Absorption spectrum and (d) optical band gap of different clam shell samples.

Figure 3. (a) XPS survey scan of CSCs at 800 °C and 1000 °C; XPS spectra of clam shell samples at: 800 °C (b) Ca2p, (c) C1s, (d) O1s, and 1000 ° C (e) Ca2p, (f) C1s, (g) O1s of CSCs.

Figure 4. Photocatalytic experiments of MB (a, b,) and CR (c, d,) with calcined catalysts at different temperatures: (a), (c) curve of removal rate with time, (b), (d) plot of log of concentration with time. Photodegradation absorption spectra of (e) MB and (f) CR solutions in the presence of clam shell powder calcined at 1000 °C.

Figure 5. Photocatalytic experiment of MB (a, b, c) and CR (d, e, f) with different doses of clam shell at 1000 °C ((a), (d) curve of absorbance with time, (b), (e) curve of removal rate with time, (c), (f) plot of log of concentration with time.

Figure 6. Photocatalytic experiment of clam shell at 1000 °C for MB (a, b, c) and CR (d, e, f); Curves of absorbance with time (a) and (d); Curves of removal rate with time (b), (e); Plots of log of concentration with time (c), (f).

Figure 7. Effects of scavenger and superoxide on MB (a, b, c) and CR (d, e, f) degradation.

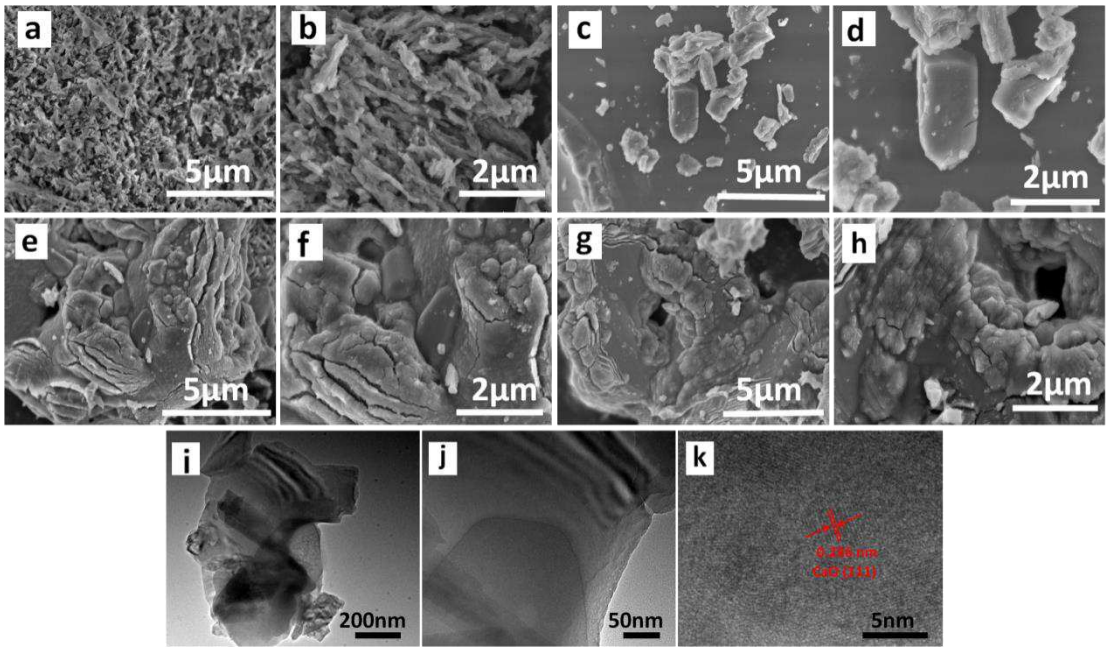

804

805 **Figure 1.** SEM images of clam shell samples: (a), (b) uncalcined; (c), (d) treated at 800 °C; (e), (f) treated
806 at 900 °C; (g), (h) treated at 1000 °C; and TEM image (i), (j) and (k) treated at 1000 °C.

807

808

809

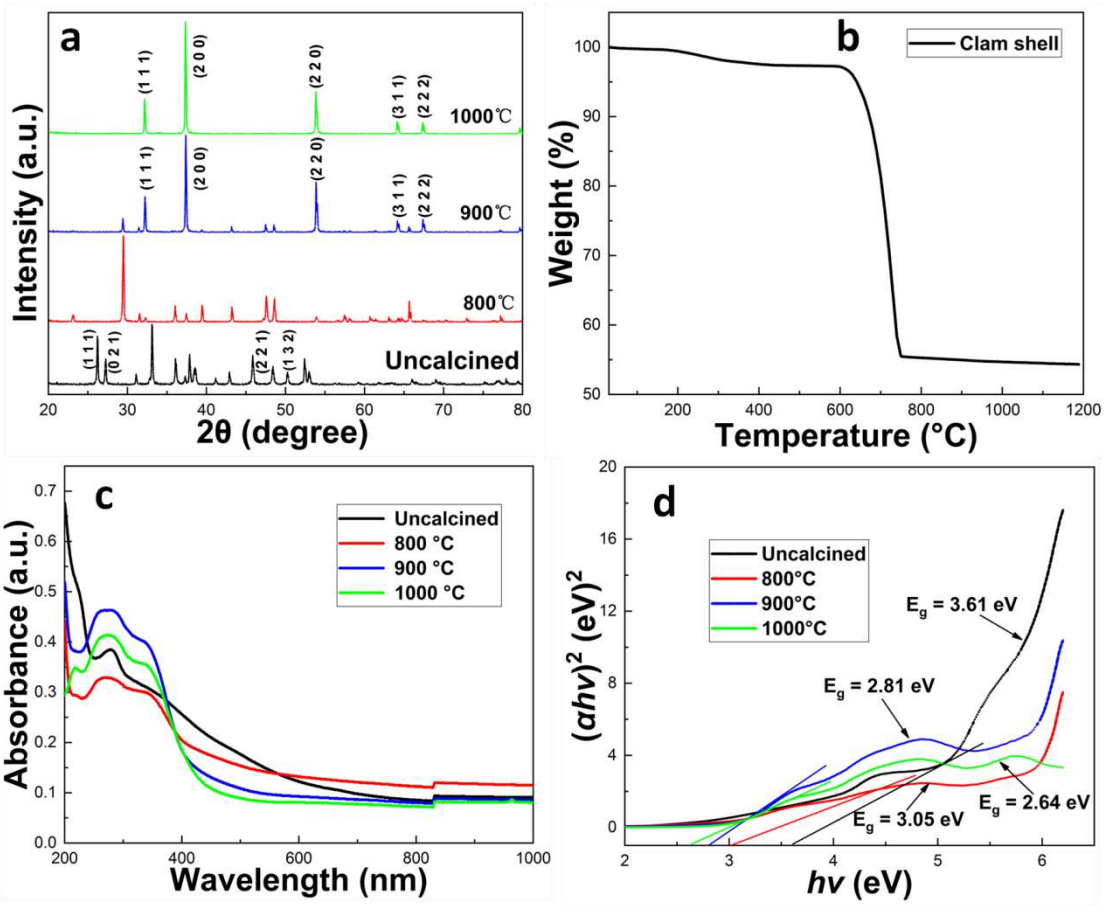

Figure 2. (a) XRD spectra of uncalcined, treated at 800, 900, and 1000 °C clam shell samples. (b) Thermogravimetric analysis of clam shell during calcination process. (c) Absorption spectrum and (d) optical band gap of different clam shell samples.

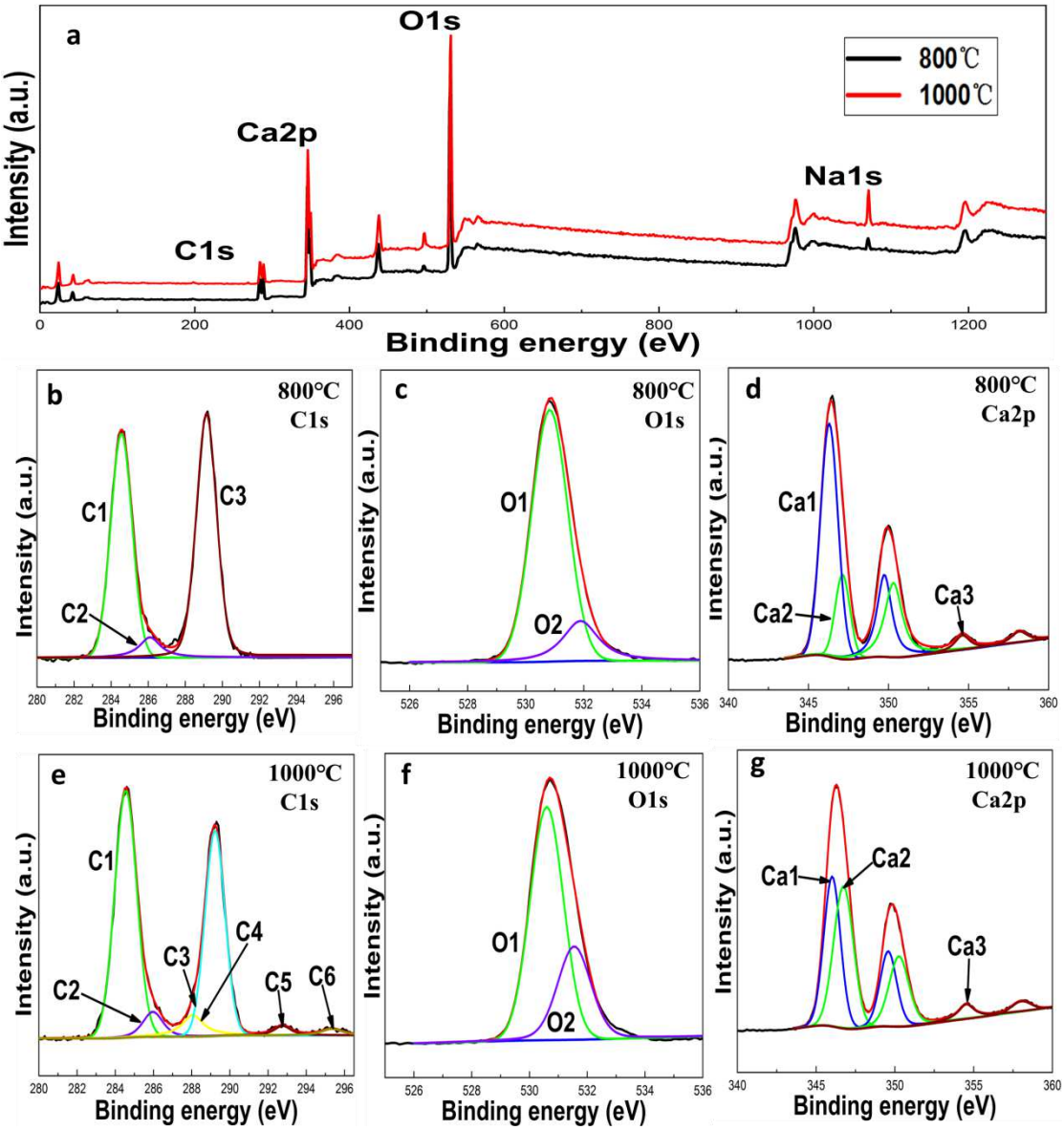

824

825 **Figure 3.** (a) XPS survey scan of CSCs at 800 °C and 1000 °C; XPS spectra of clam shell samples at:
826 800 °C (b) Ca2p, (c) C1s, (d) O1s, and 1000 ° C (e) Ca2p, (f) C1s, (g) O1s of CSCs.

827

828

829

830

831

832

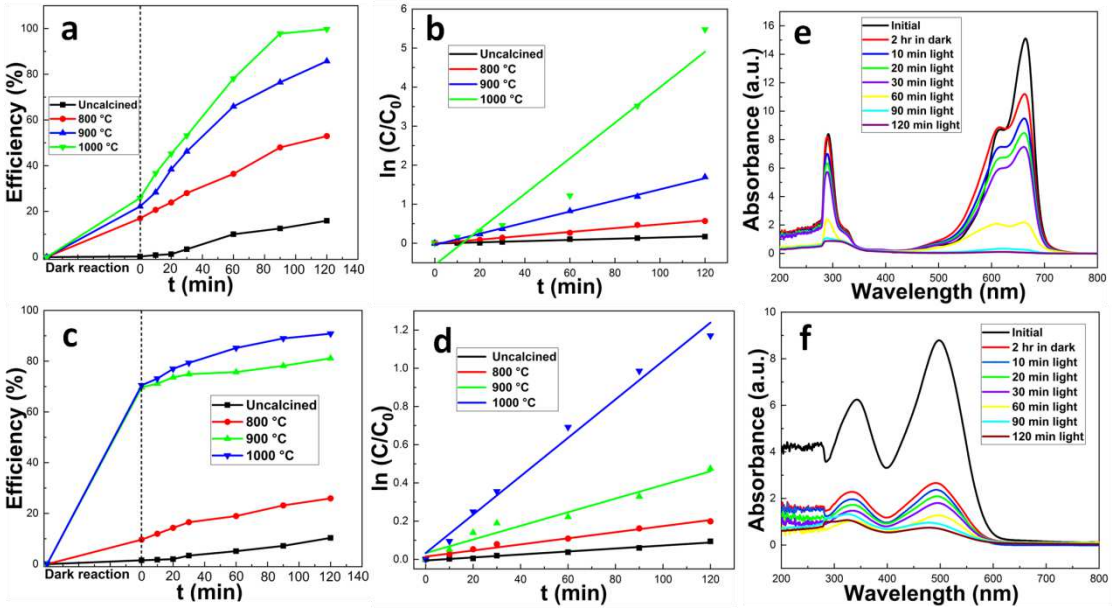

Figure 4. Photocatalytic experiments of MB (a, b,) and CR (c, d,) with calcined catalysts at different temperatures: (a), (c) curve of removal rate with time, (b), (d) plot of log of concentration with time. Photodegradation absorption spectra of (e) MB and (f) CR solutions in the presence of clam shell powder calcined at 1000 °C.

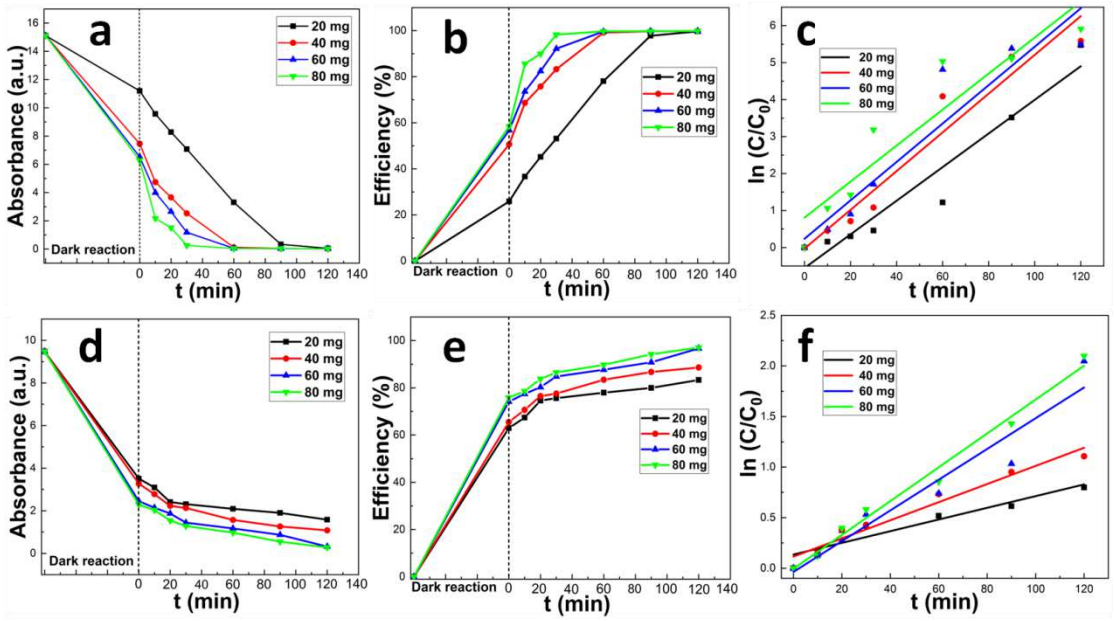

Figure 5. Photocatalytic experiment of MB (a, b, c) and CR (d, e, f) with different doses of clam shell at 1000 °C ((a), (d) curve of absorbance with time, (b), (e) curve of removal rate with time, (c), (f) plot of log of concentration with time.

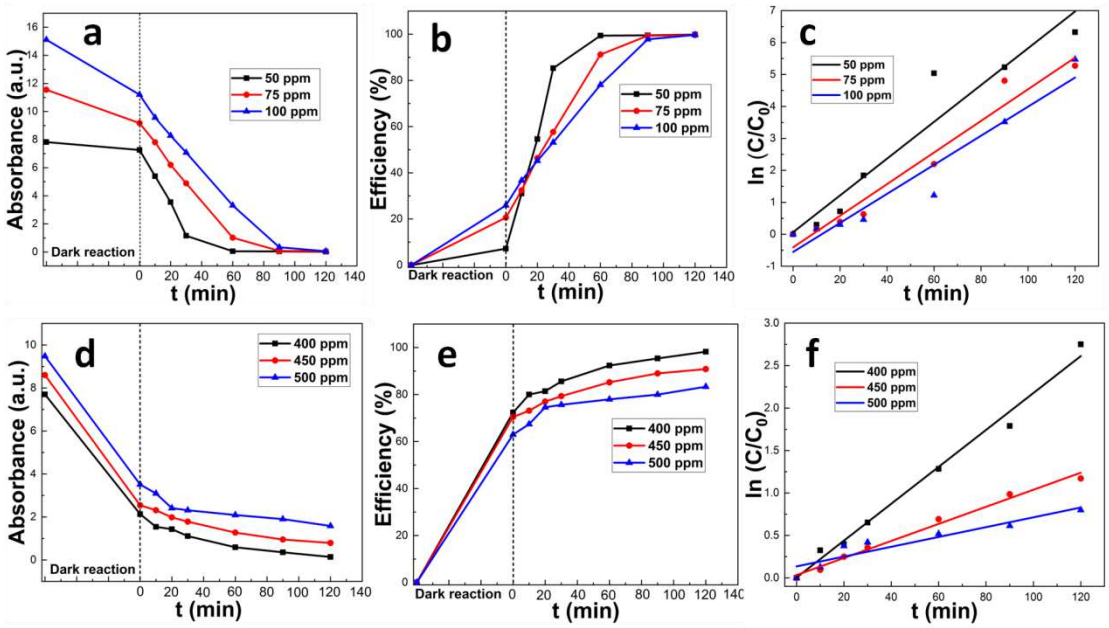

Figure 6. Photocatalytic experiment of clam shell at 1000 °C for MB (a, b, c) and CR (d, e, f); Curves of absorbance with time (a) and (d); Curves of removal rate with time (b), (e); Plots of log of concentration with time (c), (f).

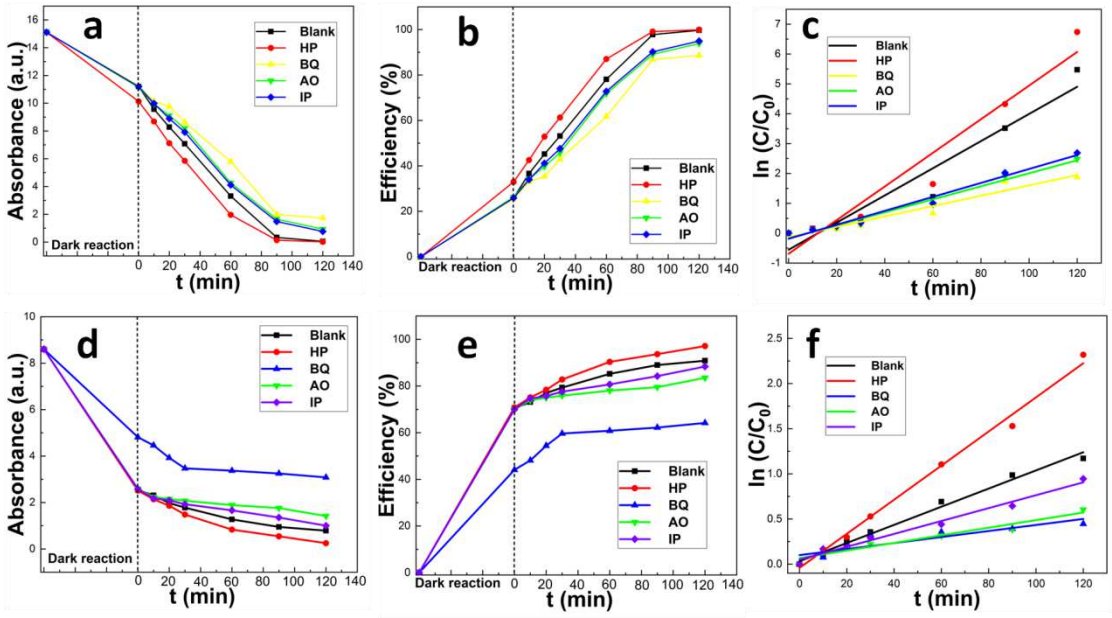

Figure 7. Effects of scavenger and superoxide on MB (a, b, c) and CR (d, e, f) degradation.

898

899 **Table 1.** Best fit photodegradation kinetic parameters for MB and CR with the four clam shells studied.

Dye	Sample	Uncalcined	800 °C	900 °C	1000 °C
MB	R^2	0.9733	0.9926	0.9973	0.9211
	k	0.0015	0.0049	0.0142	0.0455
CR	R^2	0.9779	0.9762	0.9509	0.9869
	k	0.0008	0.0016	0.0036	0.0101

900

901

902

903

904

905

906

907

908 **Table 2.** Variation in best fit degradation kinetic parameters for MB and CR with the CSC dose.

Dye	Catalyst concentration	20 mg	40 mg	60 mg	80 mg
MB	R^2	0.9211	0.9332	0.8797	0.8541
	k	0.0455	0.0524	0.0519	0.0487
CR	R^2	0.9562	0.9531	0.9228	0.9839
	k	0.0058	0.0090	0.0152	0.0167

909

910

911

912

913

914

915

916

917 **Table 3.** Variation in best fit degradation kinetics parameters for MB and CR with initial dye
918 concentration.

Dye	Dye concentration	50 ppm	75 ppm	100 ppm
MB	R^2	0.912	0.953	0.921
	k	0.058	0.049	0.045
	Dye concentration	400 ppm	450 ppm	500 ppm
CR	R^2	0.987	0.986	0.856
	k	0.022	0.010	0.006

919

920

921

922

923

924

925 **Table 4.** Variation in best fit degradation kinetic parameters of MB and CR in the presence
926 different scavengers and superoxide.

Dye	Reagent	Blank	HP	BQ	AO	IP
MB	R^2	0.921	0.931	0.937	0.976	0.976
	k	0.045	0.056	0.017	0.022	0.023
CR	R^2	0.986	0.991	0.884	0.933	0.978
	k	0.010	0.019	0.003	0.004	0.007

927

Supplementary Files

This is a list of supplementary files associated with this preprint. Click to download.

- SupplementaryMaterials.docx